Hyperchromatic structural color for perceptually enhanced sensing by the naked eye

Tahmid H. Talukdar[a], Bria McCoy[b], Sarah K. Timmins[c], Taufiquar Khan[d], and Judson D. Ryckman[a,1]

[a]Holcombe Department of Electrical and Computer Engineering, Clemson University, Clemson, SC 29634; [b]Charles H. Townes Optical Science and Engineering Summer Research Program, Clemson University, Clemson, SC 29634; [c]Department of Materials Science & Engineering, Clemson University, Clemson, SC 29634; and [d]Department of Mathematics and Statistics, University of North Carolina, Charlotte, NC 28223

Edited by John A. Rogers, Northwestern University, Evanston, IL, and approved October 8, 2020 (received for review May 16, 2020)

Colorimetric sensors offer the prospect for on-demand sensing diagnostics in simple and low-cost form factors, enabling rapid spatiotemporal inspection by digital cameras or the naked eye. However, realizing strong dynamic color variations in response to small changes in sample properties has remained a considerable challenge, which is often pursued through the use of highly responsive materials under broadband illumination. In this work, we demonstrate a general colorimetric sensing technique that overcomes the performance limitations of existing chromatic and luminance-based sensing techniques. Our approach combines structural color optical filters as sensing elements alongside a multichromatic laser illuminant. We experimentally demonstrate our approach in the context of label-free biosensing and achieve ultrasensitive and perceptually enhanced chromatic color changes in response to refractive index changes and small molecule surface attachment. Using structurally enabled chromaticity variations, the human eye is able to resolve ∼0.1-nm spectral shifts with low-quality factor (e.g., Q ∼ 15) structural filters. This enables spatially resolved biosensing in large area (approximately centimeters squared) lithography-free sensing films with a naked eye limit of detection of ∼3 pg/mm^2, lower than industry standard sensors based on surface plasmon resonance that require spectral or angular interrogation. This work highlights the key roles played by both the choice of illuminant and design of structural color filter, and it offers a promising pathway for colorimetric devices to meet the strong demand for high-performance, rapid, and portable (or point-of-care) diagnostic sensors in applications spanning from biomedicine to environmental/structural monitoring.

structural color | optics | colorimetric | sensors

The human color vision system is a highly evolved means for spatiotemporally resolving chromaticity and luminance characteristics of illuminated objects, making it one of the most powerful and inherently portable diagnostic tools in history. Similarly, the emergence of pervasive artificial imaging systems based on low-cost, portable, and high-resolution digital color cameras offers the potential to exploit luminance, chromaticity, temporal, and spatial degrees of freedom to support the on-demand analysis of sensors responding to specific input stimuli. Along this vein, a wide variety of sensors, readable by human or artificial vision, now enables the characterization of a variety of physical and chemical attributes such as temperature (1), strain (2), humidity (3), pH (4), heat transfer (5), and presence or concentration of target analytes (e.g., chemicals, biomarkers) (6–9). These so-called "colorimetric sensors" act as transducers that translate variations in input stimuli to output color variations, fostering the delivery of qualitative and/or quantitative information without the need for laboratory-grade benchtop equipment, which is traditionally more expensive, more complex or slower to operate, and less portable.

A primary challenge in developing colorimetric sensors is the task of achieving a meaningful color response, particularly for small variations of input stimuli (e.g., low analyte concentration, small environmental change, etc.). To achieve a strong color response, many colorimetric sensors rely heavily on significant physical or chemical effects such as film swelling (10–12), surface wetting (13), particle aggregation (4, 14, 15), or chemical reactions (10, 16). However, colorimetric sensing schemes based on responsive materials are not generalizable, as they are typically restricted to a niche set of stimuli and specific regimes of operation. Moreover, while the use of highly responsive materials can be effective at amplifying spectral perturbations, such approaches fail to achieve significant changes in color when the spectral perturbations in intensity and/or wavelength are small. Consequently, many leading prospective applications of colorimetric devices and sensors, such as optical biosensing for example, continue to rely heavily on noncolorimetric technologies such as those based on spectral or angular optical interrogation techniques. Overcoming the aforementioned challenges is necessary to enable the development of label-free biosensing platforms and point-of-care diagnostics readable by the naked eye and more generally, to support the realization of high-performance and spatiotemporally resolved sensors targeting a wide variety of physical stimuli.

In recent years, structural coloration has attracted considerable research and commercial interest owing to its unique ability to provide brilliant optical effects, which arise from interference and/or resonance phenomena with optical media structured on the wavelength and subwavelength scales (13, 17–20). In terms of passive structural coloration, this field has rapidly advanced alongside innovations in the design and fabrication of photonic crystals (3, 21), plasmonics (18, 22), and metasurfaces (23). However, dynamic coloration, which is required for colorimetric sensing devices and applications such as color displays, remains a

Significance

Modern scientific instrumentation and sensors are often bulky, expensive, and/or cumbersome to operate. Colorimetric sensors on the other hand offer a promising solution to these problems, as they can be analyzed with high spatiotemporal resolution by digital cameras or the naked eye. However, the performance of colorimetric sensors is typically inferior to the bulky/expensive alternatives as it can be difficult to convert small input stimulus variations into a large color response. This work introduces a means to address and overcome this problem and opens the door to types of high-performance colorimetric sensors, which are competitive with and/or offer greater functionality than the bulky/expensive alternatives.

Author contributions: T.H.T. and J.D.R. designed research; T.H.T. performed research; T.H.T., B.M., S.K.T., T.K., and J.D.R. contributed new reagents/analytic tools; T.H.T., T.K., and J.D.R. analyzed data; and T.H.T., T.K., and J.D.R. wrote the paper.

The authors declare no competing interest.

This article is a PNAS Direct Submission.

[1]To whom correspondence may be addressed. Email: jryckma@clemson.edu.

This article contains supporting information online at https://www.pnas.org/lookup/suppl/doi:10.1073/pnas.2009162117/-/DCSupplemental.

First published November 16, 2020.

considerable challenge, which has motivated numerous recent investigations into deriving dynamic coloration from both natural and artificial materials (10). Currently, most sensors based on structural coloration continue to rely primarily on broadband illumination of highly responsive materials, and the aforementioned physical effects (4, 10–15), to derive their color response. An important and open question thus arises: "How does one maximize the dynamic structural color change derived from a given change in sample properties?"

In this work, we theoretically and experimentally investigate a prospective solution that specifically seeks to address the color transduction problem of achieving a maximum perceptible color difference, ΔE_{00} (24), from a structural colorimetric sensor, which is spectrally perturbed $\Delta\lambda$ in wavelength by an input stimulus ΔS. Our high-level findings can be summarized threefold. First, we show how both the choice of illuminant and spectral design of the structural optical filter have a profound effect on the colorimetric sensitivity $\partial E_{00}/\partial\lambda$. Specifically, for broadband white light illumination, $\partial E_{00}/\partial\lambda$ is limited by an upper bound, whereas laser illumination (monochromatic or multichromatic) allows this limit to be broken. Second, multichromatic laser illumination offers fundamental benefits over monochromatic laser or narrowband illumination, including access to the largest possible colorimetric sensitivity $\partial E_{00}/\partial\lambda$ for a given spectral bandwidth or quality factor (Q), enhanced dynamic range, and a response that spans chromaticity space rather than solely the luminance coordinate. Third, we demonstrate how the enhanced $\partial E_{00}/\partial\lambda$ of a multichrome illuminated structural filter can be combined with a highly responsive material system, featuring an enhanced spectral sensitivity $\partial\lambda/\partial S$, to realize ultrahigh color transduction sensitivities $\partial E_{00}/\partial S$ and correspondingly low limits of detection (LOD) by the naked eye. Specifically, we introduce "hyperchromatic structural color" (HSC) sensors based on porous silicon thin films and characterize their functionality in performing spatially resolved label-free biosensing by the naked eye or smartphone. Despite the modest to low Q ~ 15 of our devices, the human eye is able to resolve ~0.1-nm spectral shifts and achieve a surface mass density LOD of ~3 pg/mm^2, which is competitive with industry standard sensors based on surface plasmon resonance that require spectral or angular interrogation. Our results highlight HSC, and the use of multichromatic laser illumination, as a powerful and general approach for the development of high-performance colorimetric sensors.

Approach/Framework

Sensitivity and Naked Eye LOD for Structural Color Sensors. In Fig. 1, we illustrate and compare structural colorimetric sensing schemes where an input stimulus ΔS spectrally shifts a structural optical filter by some amount $\Delta\lambda$ (relative to λ_0). The resulting dynamic structural coloration depends strongly on both the characteristics of the structural filter and the illuminant. The perceived colorimetric sensitivity can be decomposed into two partial sensitivities according to

$$\frac{\partial E_{00}}{\partial S} = \frac{\partial E_{00}}{\partial \lambda}\frac{\partial \lambda}{\partial S}. \quad [1]$$

We note that ΔE_{00}, which describes the perceived color difference, is derived per the International Commission on Illumination (CIE) 2000 standardized color differencing equation that accounts for perceptual nonuniformity in the underlying CIE color space (24). To preserve generality, the variations in input stimulus ΔS can be considered any physical, chemical, mechanical, or other attribute that perturbs the structural color filter. In the context of label-free biosensing, the sensor stimuli ΔS can be equated to a change $\Delta\sigma$ in mass surface density (picograms millimeter^{-2}) of small molecules bound to the sensor surface.

Given that naked eye perception has a color difference LOD described by the just noticeable difference, $JND \equiv \Delta E_{00} \approx 2.3$ (25), the naked eye LODs for wavelength shift $\Delta\lambda$ and sensor stimuli ΔS can be approximated according to Eqs. **2** and **3**, respectively:

$$\Delta\lambda_{JND} = 2.3\left(\frac{\partial E_{00}}{\partial \lambda}\right)^{-1} \quad [2]$$

$$\Delta S_{JND} = 2.3\left(\frac{\partial E_{00}}{\partial \lambda}\right)^{-1}\left(\frac{\partial \lambda}{\partial S}\right)^{-1}. \quad [3]$$

Hence, in modern colorimetric sensors both $\partial E_{00}/\partial\lambda$ and $\partial\lambda/\partial S$ play a critical role in the overall colorimetric response and LOD, with the spectral sensitivity $\partial\lambda/\partial S$ depending strongly on the physical properties of the sensor transduction mechanism (i.e., favoring the use of highly responsive materials) and the colorimetric sensitivity $\partial E_{00}/\partial\lambda$ depending strongly on the nature and configuration of the optical illuminant and optical filter as examined in Fig. 1.

Conventional "Chromatic" Structural Color Exhibits Bounded Sensitivity. As illustrated in Fig. 1*A*, a chromatic-type sensor may be realized, for example, by illuminating a structural color filter (e.g., Lorentzian) with a broadband or "standard illuminant" (SI). Here, the color changes in response to the filter's changing resonance wavelength, achieving a colorimetric sensitivity $\partial E_{00}/\partial\lambda \sim 1$ nm^{-1}, which is bounded to <5 nm^{-1} even in the limit of a spectral filter with an ultranarrow bandwidth (ultrahigh Q factor) in the blue spectral region (*SI Appendix* has more detail). As a result of this modest sensitivity, human vision is typically unable to detect spectral resonance shifts below ~1 to 2 nm from traditional chromatic sensors subjected to broadband illumination. This renders many colorimetric sensing tasks currently very challenging or impossible to achieve without employing the aforementioned techniques to amplify $\frac{\partial\lambda}{\partial S}$ such that in practice, $\Delta\lambda \gg 1$ nm. To illustrate chromatic sensor operation, the chromatic response arising from a $\Delta\lambda$ = 0- to 10-nm wavelength shift for two example SI illuminated Lorentzian filters (Q = 5 and 500) operating at λ_0 = 575 nm is simulated in Fig. 1*E*. In these example chromatic sensors, only a small color change from yellow toward orange is achieved.

"Luminance"-Based Structural Color with a Monochromatic Illuminant. Narrowband illumination of structural color sensors, as shown in Fig. 1*B*, has previously been demonstrated as a means for achieving high sensitivities and reducing the LOD by providing amplified luminance variations in response to small spectral perturbations (6, 7). As viewed from CIE *xyY* color space, monochromatic sensors are restricted to one-dimensional color changes along the luminance coordinate *Y*, where variations in chromaticity are strictly 0: $\Delta x = \Delta y = 0$. This restricts the Euclidean color distance to be proportional to ΔY and most importantly, restricts the magnitude of the perceived color difference ΔE_{00}.

Hence, while luminance-based sensors offer access to theoretically unbounded increases in sensitivity $\partial E_{00}/\partial\lambda$ (*SI Appendix* has additional detail; e.g., shown mathematically via the scale factor *a* shown in Fig. 1*B*), they fundamentally fail to exploit the eye's highly evolved ability to easily discriminate chromatic colors owing to the differential spectral properties of individual human photoreceptors and instead, rely on single-ended intensity information. Similarly, when sensing is performed with a color camera, a narrowband illuminated sensor fails to leverage the unique spectral characteristics of complementary metal–oxide–semiconductor (CMOS) red, green, and blue (RGB) subpixels (26). This also limits the dynamic range of the sensor. To maximally leverage the advanced detection capabilities offered by human color perception and the multiplexed sensors inherently embedded in CMOS color cameras, it is desirable to leverage the

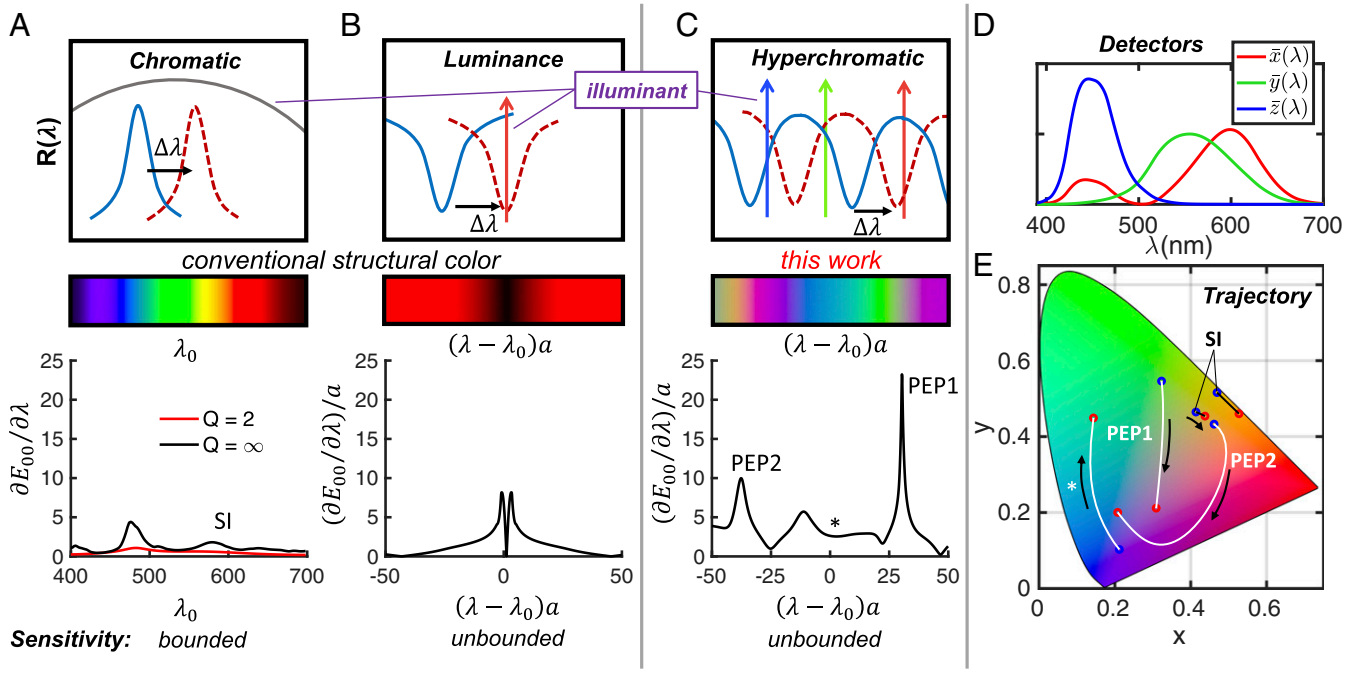

Fig. 1. Overview of colorimetric sensing schemes wherein a wavelength shifting structural color filter induces a perceived change in color with sensitivity $\partial E_{00}/\partial\lambda$: (*A*) chromatic sensing with a white light SI, illustrated for Lorentzian filters with varying Q factors; (*B*) luminance sensing with a narrowband light source, illustrated with a single ($n = 1$) monochromatic laser; and (*C*) hyperchromatic sensing (introduced in this work) with a multichromatic laser (e.g., $n = 3$, RGB) combined with an optical filter (e.g., Fabry–Perot interferometer). Local maxima in the function $\partial E_{00}/\partial\lambda$ correspond to PEPs. (*D*) Spectral shape of the color matching functions associated with color perception. (*E*) The simulated chromaticity trajectories of example sensors in response to $\Delta\lambda = 0 - 10$ nm, including: SI illuminated chromatic sensors (Q = 5 and 500) and hyperchromatic sensors realized from thin-film Fabry–Perot interferometers with thickness $D = D_0\left(m \pm \frac{1}{3}\right)$, where $m = 1$ and $a = 1$ for PEP1 and $m = 4$ and $a = 3.25$ for PEP2; and $\Delta\lambda = 0 - 1.0$ nm, where $m = 32$ and $a = 24.25$ for the asterisk (*).

chromatic degrees of freedom and derive a highly chromatic response from small spectral perturbations. As discussed above, however, such a task inherently cannot be achieved with either broadband or monochromatic optical illumination.

HSC with a Multichromatic Laser Illuminant (This Work). The use of a multichromatic ($n \geq 2$) laser illuminant in combination with an appropriately tailored structural color filter is a promising solution to the aforementioned limitations. This scheme, which we refer to as "hyperchromatic structural color" or HSC, offers an enhanced "hyperchromatic" response within the current chromaticity space, theoretically unbounded sensitivity $\partial E_{00}/\partial\lambda$, and allows the design of a wide range of dynamic color trajectories and transitions. This fosters the development of HSC-based sensors featuring enhanced dynamic range and/or an enhanced sensitivity and improved LOD vs. what can be achieved with either a luminance or conventional chromatic-based sensor. In this study, we employ a multichromatic laser illuminant composed of $N = 3$ lasers with blue, green, and red wavelengths $\lambda_b = 450$ nm, $\lambda_g = 524$ nm, and $\lambda_r = 635$ nm, respectively (unless otherwise stated). The structural color filter in the HSC scheme should be designed such that the spectral perturbation $\Delta R(\lambda)$ arising from the sensor stimuli is both large in magnitude and nonuniform across the three laser wavelengths. In principle, these requirements can be achieved with a wide variety of optical filter sensor designs to yield a wide variety of structurally engineered chromatic responses. In this work, we choose a reflective optical filter based on a thin-film Fabry–Perot interferometer on a silicon substrate (27). Our film thicknesses are chosen to be near a "magic" thickness $D = \frac{\pi c}{n_g\,\Delta\omega\,cos\phi}\left(m \pm \frac{1}{3}\right)$, where n_g is the group index, ϕ_i is the angle of incidence, c is the speed of light, $\Delta\omega$ is the nominal frequency spacing between adjacent laser frequencies, and m is an integer. This configuration avoids the "antimagic" thicknesses $mD_0 = m\frac{\pi c}{n_g\,\Delta\omega\,cos\phi_i}$, wherein the RGB intensity variations are in phase and an achromatic sensor response occurs (*SI Appendix*, Fig. S1), and instead, establishes operation at or slightly detuned from a condition where reflected RGB intensity exhibits a three-phase variation vs. wavelength shift (*SI Appendix*, Fig. S2).

In HSC sensing, there are multiple complementary pathways for enhancing $\partial E_{00}/\partial\lambda$. One approach, which is common also to luminance-type sensors, is to increase the Q factor and finesse of the optical filter utilized in the sensor (e.g., increase the scale factor a shown in Fig. 1). A second approach is to engineer a chromatic color transition (under a given Q factor and finesse), which provides a perceptually enhanced sensitivity when crossing through a "perceptual enhancement point" (PEP). We define a PEP as an operating point in chromaticity space where there is a significant local maxima in the function $\partial E_{00}/\partial\lambda$. Here, the amplified sensitivity represents the ability to perform sensing with stronger and more perceptible color differences and originates from achieving strong differential variations in RGB intensity, which promote strong differential signals across the multiple distinct photoreceptors of the eye and/or color camera. For example, in Fig. 1 *C* and *E*, "PEP1" reveals that a significant enhancement to $\partial E_{00}/\partial\lambda$ can be achieved at the midpoint between a structurally enabled green to magenta color transition. This transition, which "pushes" green intensity down while simultaneously "pulling" blue and red intensity up, is qualitatively analogous to "push–pull" interferometry and is found to be easier to discriminate by human vision than a luminance-only color transition between dark and light red. Hence, the hyperchromatic sensitivity $\partial E_{00}/\partial\lambda$ exhibited near PEP1 is found to exceed the luminance sensitivity by a factor of approximately three (Fig. 1*B*) when both structures utilize the same type optical filter with exactly the same

finesse and quality factor. In this case, to match the sensitivity of PEP1 exhibited in the hyperchromatic scheme, the luminance-based sensor would require a Q factor approximately three times larger than the hyperchromatic structure, such that the scale parameter a indicated on the Fig. 1*B* axes is increased by threefold. In this same fashion, a hyperchromatic sensor could also operate without working near a PEP (i.e., near the region indicated by the asterisk in Fig. 1*C* and demonstrated in Fig. 1*E*). However, matching the sensitivity exhibited by PEP1 would require the Q factor to be elevated by ∼5 to 10 times.

Experimental Scheme

HSC Sensors from Porous Silicon. In this work, we experimentally demonstrate HSC sensing using porous silicon thin-film interferometers as the structural color filters. Porous silicon has been widely investigated in sensing applications, where it attractively offers large changes in effective refractive index (RI) in response to the infiltration, adsorption, or immobilization of chemical and biochemical species (28, 29). In this context, the sensor stimuli ΔS are equated to a change $\Delta\sigma$ in mass surface density (picograms millimeter^{-2}) of small molecules bound to the sensor surface. Porous silicon offers ultrahigh $\partial\lambda/\partial\sigma$ values on the order of ∼10 to 100 picometer/(pg mm^{-2}) (30, 31), which are up to two orders of magnitude larger than other photonic or plasmonic platforms (32, 33). The enhanced $\partial\lambda/\partial\sigma$ sensitivity is then combined with an ultrahigh $\partial E_{00}/\partial\lambda$ sensitivity using our HSC technique to effectively amplify both sensitivity terms of Eq. **1** and enable ultrahigh $\partial E_{00}/\partial\sigma$ values. This offers the prospect for developing colorimetric label-free biosensors capable of unprecedently low LODs that are detectable by the naked eye.

The experimental configuration is depicted in Fig. 2*A*. An RGB laser is coupled into a 170-μm-core diameter multimode fiber (MMF), which illuminates the planar sensor chip (Fig. 2*B*) using a collimating lens. The specularly reflected light projects onto a white diffuser screen (Thorlabs EDU-VS1) to enable imaging by eye and by a smartphone camera (iPhone 6). Typically, this type of laser illumination would lead to significant image distortions owing to speckle noise (34). Here, we devised a solution to the speckle problem based on 1) use of specialty light diffusing MMF (Versalume Corning Fibrance) and 2) mechanically shaking the fiber during image or video capture. This technique enables high-resolution imaging of the sensor surface with minimal speckle artifacts (*SI Appendix*, Figs. S3 and S4 have more detail).

Results

Proof-of-Concept Demonstration. We fabricated mesoporous silicon thin films with ∼75% porosity and ∼40-nm mean pore diameter in thicknesses of ∼1,140 nm ("recipe A") or ∼1,250 nm ("recipe B") to use as the sensing element (Fig. 2*C*). At normal incidence, these thin-film Fabry–Perot interferometers exhibit free-spectral ranges (FSRs) of ∼71.75 and ∼67.3 nm, at the green laser wavelength, for recipes A and B, respectively, and extinction ratios of ∼10 dB near all three laser wavelengths (*SI Appendix*, Figs. S4 and S5 have details). To illustrate the hyperchromatic sensing scheme, we first expose the thin-film sensors to water vapor, which can be delivered directly from human breath or using a portable nebulizer. When the sensor is freshly anodized, the internal porous silicon surface is strongly hydrogen terminated and very hydrophobic. In such a case, water vapor is unable to adsorb inside the pores or deposit on the internal surface, resulting in no significant RI change or spectral change of the thin film. A video recording of such a sensor's response to water vapor exposure confirms that no color change and hence, no vapor deposition are observed (Movie S1).

The porous silicon films are oxidized in air ambient at 500 °C for 10 min, resulting in a hydrophilic SiO_2 surface that allows both water vapor adsorption and glass surface chemistry to be utilized. Fig. 1*D* illustrates the normal incidence reflectance spectra taken from an oxidized thin-film sensor as it responds to water vapor adsorption inside the pores. As water molecules deposit on the internal pore surface, the effective RI of the film increases from ∼1.36 up to ∼1.58, resulting in a large ∼72-nm red shift in the reflectance spectrum as measured at $\lambda = 575$ nm. When the same vapor adsorption is applied to our sensor chip in the HSC scheme, a significant change in the structural color and a color trajectory is observed. Desorption of the water vapor was observed to occur on a timescale of ∼30 s under ambient conditions, and hence, the water adsorption/desorption process can be cycled on demand and observed with high spatiotemporal resolution using the smartphone video camera. Videos of water vapor exposure on recipe A and recipe B samples delivered via human breath and portable nebulizer, respectively, are included as Movies S2 and S3. The chromaticity response at the middle of a recipe B-type sample is then analyzed over the course of a water vapor adsorption cycle and reported in Fig. 2*E* alongside images from four selected frames (Fig. 2 *F*, *I–IV*). These images illustrate the hyperchromatic response of the device, which transitions from (Fig. 2 *F*, *I*) reddish magenta to (Fig. 2 *F*, *II*) blueish magenta and (Fig. 2 *F*, *III*) bright green before (Fig. 2 *F*, *IV*) crossing toward magenta. This final transition, which reveals a color gradient in the sample as captured in frame *IV* of Fig. 2*F*, illustrates the sensor operating in the vicinity of a PEP similar to the PEP1 simulation from Fig. 1*C*. The transition from green to magenta produces a color change that is visually highly perceptible, hence yielding a perceived color difference that is much larger than the yellowish green to blueish green transition occurring in frame *III* of Fig. 2*F*, wherein the same gradient is less detectable.

Mapping Performance across a PEP. As reported in Fig. 3, we simulated and experimentally mapped the color trajectory and colorimetric sensitivity, $\partial E_{00}/\partial\lambda$, for both recipe A and recipe B. Despite the conceptual similarity of the two sensors, the different FSR for each sensor is predicted and shown to give rise to substantially different characteristics. For example, recipe A operates with a magic thickness, and its color trajectory makes a clockwise orbit through chromaticity space as the filtered RGB laser intensities vary in three-phase manner. Perceptual enhancement is achieved near inflections in the three-phase RGB variation. Recipe B, meanwhile, is detuned from the three-phase configuration such that red and blue intensity variations are approximately in phase with each other while antiphase with green, thus enabling the green to magenta color transition, which is visually very distinct and associated with a strong PEP.

As illustrated in Figs. 3 *C* and *D* and 4, we experimentally characterized the colorimetric sensitivity $\partial E_{00}/\partial\lambda$ of the two different HSC filter designs, recipe A and recipe B, in their as fabricated "initial" state and as they are tuned to achieve perceptual enhancement. We also measured their colorimetric sensitivity toward small molecule surface attachment, $\partial E_{00}/\partial\sigma$, as well as the corresponding LOD for both $\Delta\lambda$ and $\Delta\sigma$. To enable this sensor characterization, we exposed the sensors to prototypical small molecule surface attachment of varying surface coverage and complemented our colorimetric measurements with spectral characterization of the sample's spectral shift. To achieve variable surface adlayer attachment with a representative small molecule, we exposed samples to various concentrations and durations of silanization using 3-aminopropyltriethoxysilane (3-APTES). The maximum applied exposure condition of 4% 3-APTES in dry toluene, followed by rinsing in deionized water, deposits a surface-attached adlayer inside the pores, which yields a wavelength shift $\Delta\lambda = 34$ nm (quoted from 575 nm) corresponding to a thin-film effective RI change $\Delta n = 0.106$. Given an adsorbed adlayer RI $n \approx 1.46$ (30), this optical response corresponds to an ∼1-nm-thick surface-attached adlayer coating the internal pore surface, equivalent to an attached mass surface density $\Delta\sigma = 948$ pg mm^{-2}. Shorter silane exposure durations and concentrations, as small as

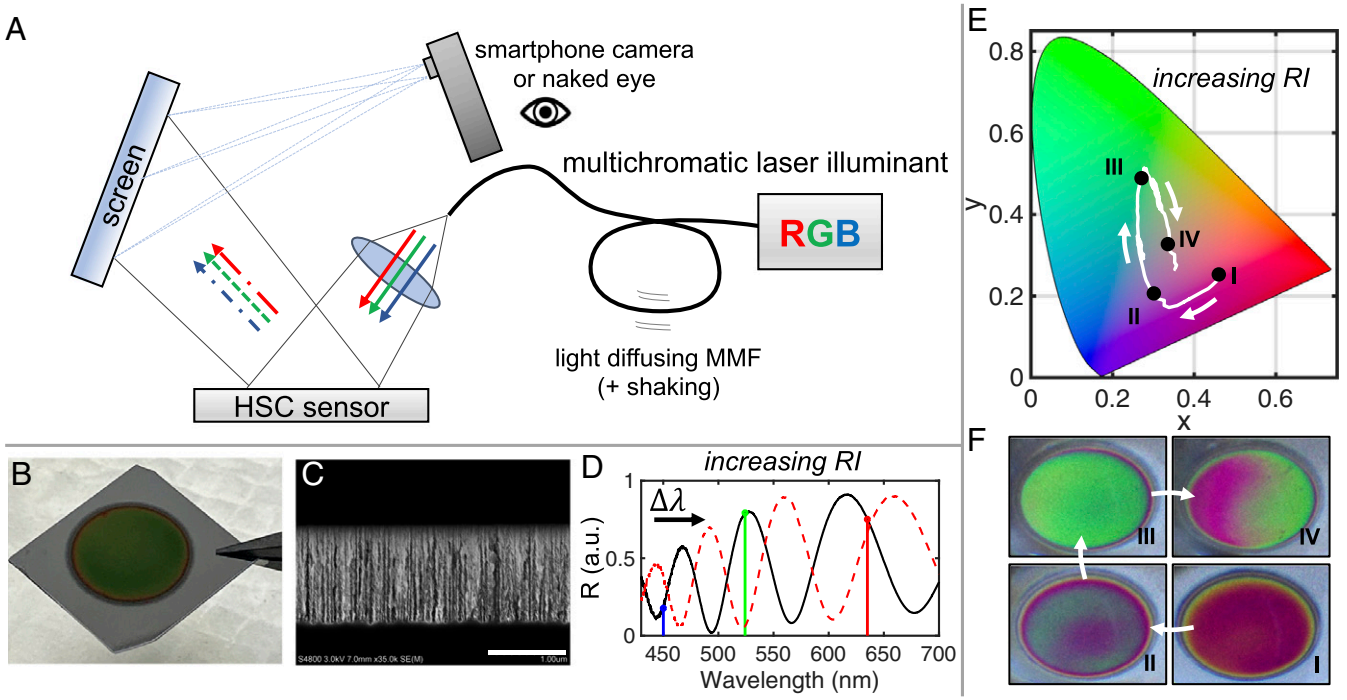

Fig. 2. (*A*) Schematic illustration of the experimental setup. (*B*) Photograph of the porous silicon sensor chip. (*C*) Cross-sectional SEM image of the porous silicon film. (*D*) Reflectance spectrum and observed shift resulting from vapor adsorption. (*E*) The color change trajectory in the chromaticity color space during the vapor adsorption process. *F*, *I–IV* shows sensor images at various frames in the color trajectory.

0.001% for 5 s, enable sub-monolayer (<1-nm) coverage to be delivered and hence, smaller values of $\Delta\sigma$, Δn, and $\Delta\lambda$ to be induced and then sensed. The wavelength shifts, $\Delta\lambda$, reported in Fig. 4 are extracted from the reflectance spectra measured before and after 3-APTES treatment. The perceived color change ΔE_{00} is measured as the color difference captured by the smartphone between exposed and unexposed regions in close proximity on the same sample.

Measurements of recipe A reveal that it is initially yellow in color (Fig. 4) and that small $+\Delta\lambda$ perturbations induce a color change toward a more reddish yellow, consistent with the trajectory predicted in Fig. 3*A*. In its initial state, the colorimetric sensitivity is below $\partial E_{00}/\partial\lambda \sim 1$ nm^{-1}. This moderate sensitivity, which is comparable with standard chromatic sensors, makes it nearly impossible for the naked eye to discern the small $\Delta\lambda \sim 3$-nm shift resulting from the ~5-s 0.001% 3-APTES exposure, which was isolated to the spot indicated by the white arrows in Fig. 4. However, if the optical filter is tuned away from its initial state by red shifting the filter spectrum, then the perceived color contrast between the partially silanized and unexposed regions can be enhanced as the chromatic response approaches a PEP. To globally shift the filter spectrum, we expose the postsilanized samples to water vapor as earlier demonstrated in Fig. 2 *E* and *F*. Deposition of water vapor inside the pores gradually increases the effective RI of the entire film and allows the sample to be quickly and easily scanned across a large colorimetric trajectory, and thus swept across a PEP, analogous to how spectral or angular scanning may be used to sweep across a photonic or plasmonic resonance. Smartphone camera videos corresponding to the vapor exposure cycle applied to recipe A (Movie S4) and recipe B (Movie S5) were recorded for the two samples with the smallest $\Delta\lambda$ silane exposure. Tracking the color contrast between unsilanized and partially silanized spots on the sensor surface, for an entire vapor adsorption cycle (or RI sweep), allows the sensitivity $\partial E_{00}/\partial\lambda$ to be mapped as a function of the sample's reference (unsilanized) chromaticity coordinates as shown in Fig. 3 *C* and *D*. For recipe A, multiple local maxima in $\partial E_{00}/\partial\lambda$ are experimentally observed as shown in Fig. 3*D*, which are consistent with the PEPs predicted in simulation (Fig. 3*B*). At each PEP, the colorimetric sensitivity $\partial E_{00}/\partial\lambda$ is enhanced more than three times relative to the initial state. This enables the silane exposure spot with small $\Delta\lambda \sim 3$ nm to become detectable by the naked eye as shown in Fig. 4, *Top*.

Recipe B exhibits an initial sensitivity $\partial E_{00}/\partial\lambda \sim 6$ nm^{-1}, making the minimal silane exposure spot faintly visible to the naked eye without any filter tuning. Performing a vapor adsorption cycle (or RI sweep) on recipe B initially lowers the sensitivity to $\partial E_{00}/\partial\lambda \sim 1$ nm^{-1} when tuned into the green color region but subsequently enhances the sensitivity to a maximum of $\partial E_{00}/\partial\lambda \sim 21$ nm^{-1} as the sensor passes through its PEP. As shown in Fig. 3*E*, the colorimetric sensitivity peaks sharply exactly at the center of the green to magenta transition as predicted. Both the chromatic response trajectory and sensitivity of the sensors are in good agreement with simulation. It should be noted that the color trajectories analyzed by smartphone are limited to the standard red, green, and blue (sRGB) color gamut of the digital images (26), while the true color trajectory observed by the naked eye can extend outside sRGB to the full gamut of CIE *xy* chromaticity space (*SI Appendix* has more details).

When recipe B is tuned to the green/magenta PEP, the large colorimetric sensitivity $\partial E_{00}/\partial\lambda = 21$ nm^{-1} effectively enables the human eye to resolve spectral variations as small as $\Delta\lambda_{JND} = 0.11$ nm (per Eq. **2**). As a result, the submonolayer 3-APTES exposure spot with $\Delta\lambda = 2.7$ nm is clearly visible by the naked eye as shown in Fig. 4, *Middle* and produces a distinct color change $\Delta E_{00} = 57$. This large color response, which is >20 times greater than the *JND*, arises from submonolayer binding of small molecules estimated at $\Delta\sigma = 75$ pg mm^{-2}, or the optical equivalent of a surface adsorbed adlayer with $n = 1.46$ and an effective adlayer thickness $t = 0.8$ Å. In this sensor, the visible color is dramatically altered by

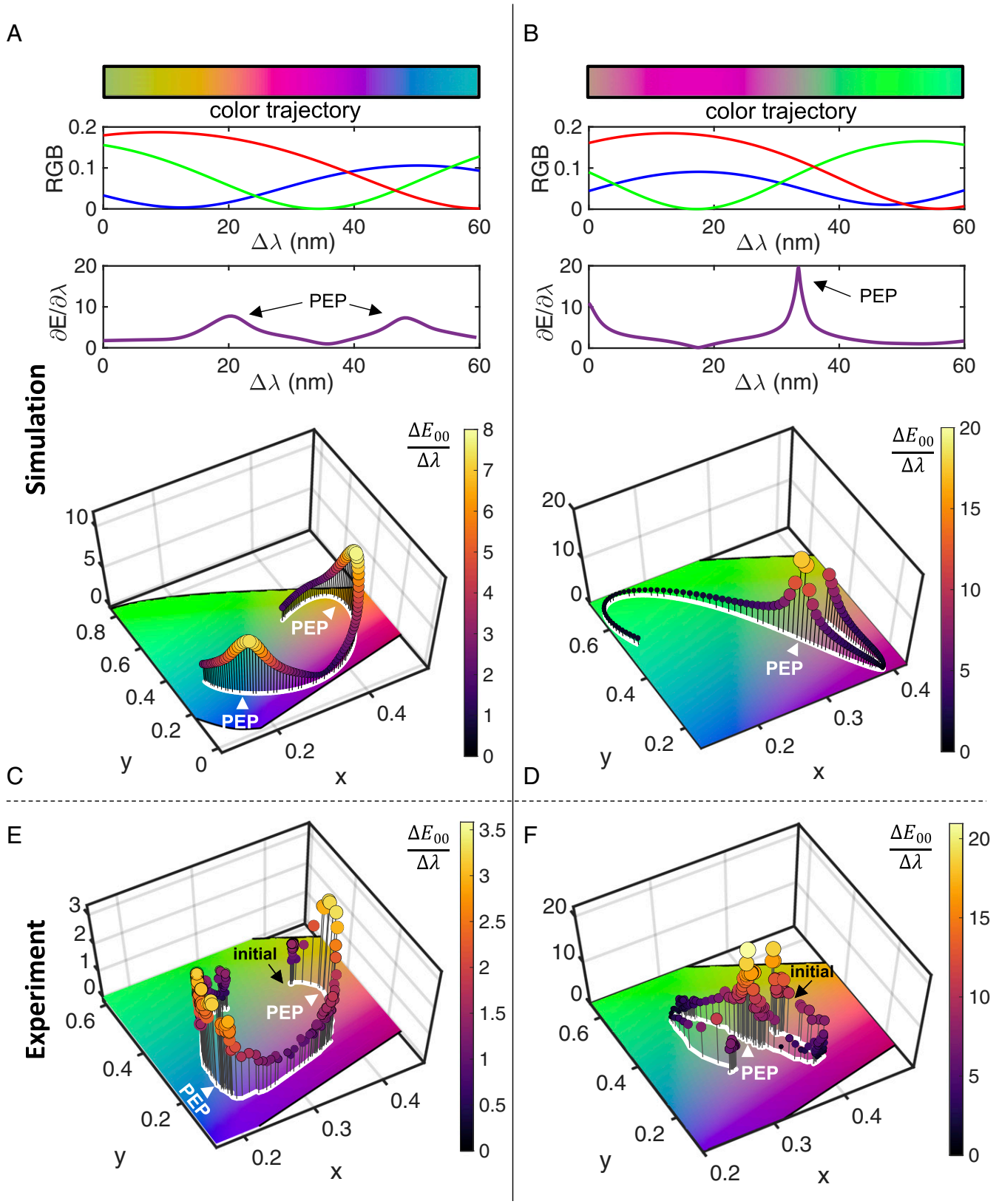

Fig. 3. Simulated color trajectory and relative intensity (arbitrary units) variation for the reflected RGB lasers vs. wavelength shift $\Delta\lambda$ and the corresponding colorimetric sensitivities for (*A*) recipe A and (*B*) recipe B. (*C* and *D*) Simulated colorimetric sensitivity and variation through chromaticity space for recipe A and recipe B, respectively. (*E* and *F*) Experimentally measured colorimetric sensitivity and variation through chromaticity space for recipe A and recipe B, respectively. PEP labels indicate locations of PEPs.

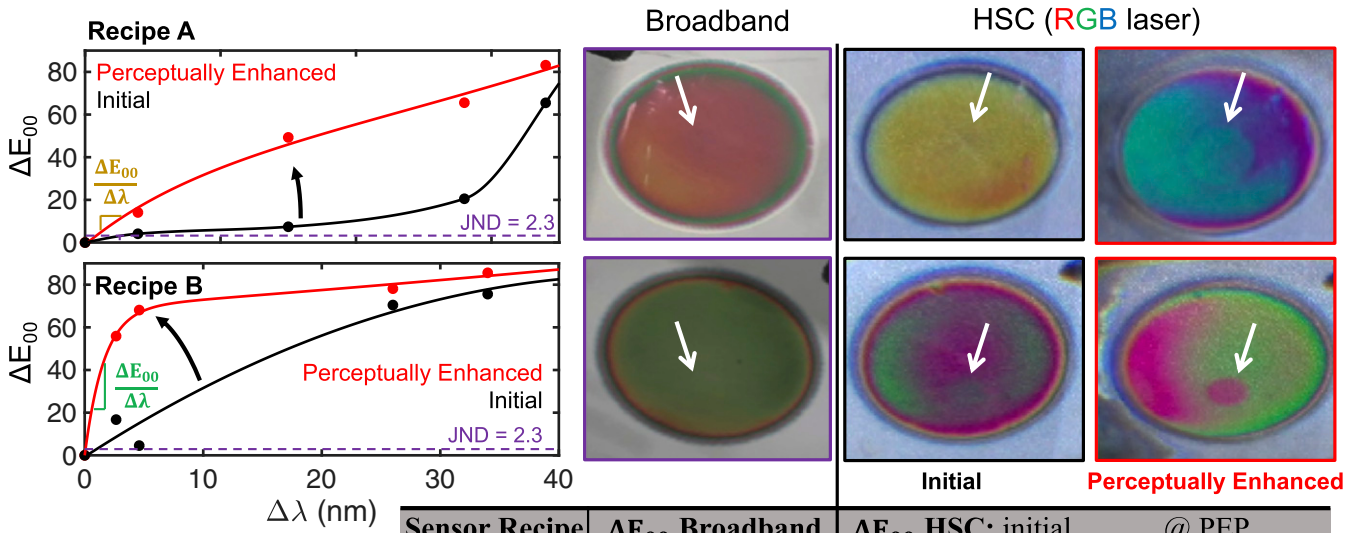

Sensor Recipe	ΔE_{00} Broadband	ΔE_{00} HSC: initial	@ PEP
A, $\Delta\lambda$ = 3 nm	~1	1.6	**12.6**
B, $\Delta\lambda$ = 2.7 nm	~1	7.5	**57**

Fig. 4. (*Left*) Initial and perceptually enhanced color change ΔE_{00} vs. wavelength shift $\Delta\lambda$ for (*Top*) recipe A and (*Middle*) recipe B. (*Right*) Smartphone images of the sensors under broadband white light illumination as compared with initial and perceptually enhanced images taken under the HSC scheme. (*Bottom*) A table summarizing the observed color change. White arrows indicate the location of submonolayer 3-APTES exposure.

subangstrom-scale variations in surface attachment properties, and in principle, the naked eye could detect the deposition of an $n = 1.46$ surface adlayer with a minimum resolution of $t_{JND} = 0.03$ Å.

LODs and Literature Comparison. These experiments indicate that recipe A achieves a maximum label-free surface sensitivity $\partial E_{00}/\partial\sigma = 0.12$ pg^{-1} mm^2, while recipe B achieves $\partial E_{00}/\partial\sigma = 0.75$ pg^{-1} mm^2. Given that the naked eye LOD is set by the *JND*, the naked eye LODs for recipe A and recipe B are estimated at $\sigma_{JND} = 18$ pg mm^{-2} and $\sigma_{JND} = 3$ pg mm^{-2}, respectively. These values are competitive with or lower than the LOD, ~10 pg mm^{-2}, of conventional surface plasmon resonance techniques (35, 36), which require spectral or angular interrogation, yet our sensor achieves label-free color changes that are detectable directly by the naked eye.

As summarized in Table 1, our HSC scheme enabled demonstration of an enhanced colorimetric sensitivity $\partial E_{00}/\partial\lambda$, which is ~7 to 30 times higher than recently reported structural color-based sensors (6, 7, 37). Combined with the use of a high-sensitivity porous medium, our structure enhances both terms of Eq. **1** to realize very large colorimetric sensitivities toward surface attachment $\partial E_{00}/\partial\sigma$. Hence, the naked eye LOD for surface mass density σ_{JND} and equivalent surface adlayer thickness t_{JND} in our structure are ~30 to 1,000 times lower than the recent literature examples of structural color-based surface adlayer label-free biosensors (6, 7, 37). Given that the sensitivity, $\partial E_{00}/\partial\lambda$, of the HSC technique is theoretically unbounded and that the Q factor and finesse of our optical filter can be significantly increased in future work, this sensing platform offers a promising route toward achieving colorimetric label-free biosensors with naked eye LODs well below 1 pg mm^{-2}.

Spatially Resolved Label-Free Biosensing by the Naked Eye or Smartphone. Next, we performed a spatially resolved sensing experiment wherein a local surface functionalization and biotinylation are applied as shown in Fig. 5. This experiment is performed with the same sensor recipe as recipe A in order to demonstrate and study the spatially resolved sensing capabilities offered by the HSC technique. First, local silanization (4% 3-APTES) is locally applied to an ~8-mm-diameter spot on the sensor surface. The sample is then locally exposed to 20 μL of ~0.0022 g/mL sulfo-*n*-hydroxysuccinimide (NHS)-biotin for 20 min with the drop partially overlapping the silanized region. Note that after each exposure, the surface is rinsed with deionized water and dried under airflow. In the overlapping "A + B" exposure region, cross-linking occurs as the sulfo-NHS–activated biotin reacts with surface amino groups to form amide bonds yielding a locally biotinylated surface.

A large color change is observed in the regions where the sensor surface is functionalized, as indicated by the smartphone camera images shown in Fig. 5. Silanization is observed to induce a median net color difference $\Delta E_{00} = 31$ relative to the reference image "REF," while biotinylation induces $\Delta E_{00} = 41$ relative to the postsilanization image A. Nonspecific adsorption of sulfo-NHS-biotin is also detectable by the naked eye, exhibiting a color difference $\Delta E_{00} = 8$. This experiment further demonstrates how HSC sensing offers a simple means for obtaining spatially resolved sensing information without requiring highly specialized image scanning or mapping techniques such as hyperspectral imaging (38–40), or resonance scanning (41). This opens possibilities for performing multiplexed sensing via colorimetric micro- or macroarrays readable by microscope cameras, smartphones, or the naked eye.

Spatially Resolved Visualization of Biotin–Streptavidin Binding. Next, we demonstrate spatially resolved specific detection of the biotin–streptavidin interaction, visualized directly by the naked eye or smartphone. As shown in Fig. 6, we fabricated three modified "recipe C"-type samples (*Materials and Methods*), which were then silanized with 3-APTES to achieve an amine (A in Fig. 6) functional surface. Two samples were then diced in half, with only one-half receiving biotinylation (B in Fig. 6). To promote stability of the surface after streptavidin binding, here we utilized NHS-polyethylene-glycol (PEG_4)-biotin (*Materials and Methods*). Next, streptavidin (S in Fig. 6) was locally applied to the samples with both amine and biotin functional surfaces. Specific interaction is clearly observed as shown in Fig. 6, *i* and *ii* as a large

Table 1. Comparison of selected structural color surface attachment label-free biosensors from the recent literature and this work

Source	Scheme	$dE_{00}/d\lambda$, nm^{-1}	$d\lambda/d\sigma$, nm/(pg mm^{-2})	$dE_{00}/d\sigma$, 1/(pg mm^{-2})	$\Delta\lambda_{JND}$, nm	σ_{JND}, pg mm^{-2}	t_{JND}, Å
Yanik et al. (6)	Luminance	3.2*	~2.3×10^{-3}	~7.4×10^{-4}	~0.72	~3,100	~33
Gartia et al. (37)	Chromatic	1.3*	~1.4×10^{-2}	~2.2×10^{-2}	~1.77	~104	~1.1
Cao et al. (7)	Luminance	0.7*	~3.5×10^{-2}	~2.45×10^{-2}	~3.29	~94	~1
This work	HSC	21	3.5×10^{-2}	0.745	0.11	3.1	0.033

This table summarizes the colorimetric and spectral sensitivities to surface attachment as well as the naked eye LODs for wavelength shift, $\Delta\lambda_{JND}$; mass surface density, σ_{JND}; and the equivalent surface attachment (n = 1.46) thickness, t_{JND}. (*SI Appendix* has additional details.)
*Determined from simulation.

color change is only visible on the biotinylated surface. A small color change is faintly detectable for the amine-only surface as indicated in Fig. 6, *v* and *vi*; however, the hue, Δh_{ab}, moves in the opposite direction as the biotinylated surface, which is indicative of a small degree of nonspecific surface corrosion or net debinding of surface molecules.

By varying the streptavidin exposure time between 1 and 45 min, we illustrate how the sensor can track changes in submonolayer surface coverage of streptavidin. Here, the entire sensor surface is biotinylated, and streptavidin is iteratively applied to four spots on the sensor surface beginning first with the 1-min exposure, indicated in Fig. 6, *iii* by the white arrow, and progressing clockwise with exposure durations of 10, 20, and 45 min. A control spot containing phosphate-buffered saline (1X PBS) with no streptavidin was exposed in the very center of the sample for 45 min. Color difference maps shown in Fig. 6, *iv* report the spatially resolved variation in ΔE_{00} relative to a reference image taken before surface attachment, and Fig. 6, *vi* reveals the chromaticity values and trajectory of the sensor at each step. As the streptavidin exposure time and surface attachment increase, the color of the sensor makes a clockwise orbit around chromaticity space. For the 45-min exposure spot, the color variation nearly completes an entire orbit around chromaticity space, which highlights the hyperchromatic response of the sensor as well as its large dynamic range. This proof-of-concept demonstration further illustrates how spatially resolved and specific label-free detection of small molecules can be performed by the naked eye.

HSC Using a Portable Handheld RGB Laser Module. A key advantage of colorimetric sensors over conventional benchtop laboratory equipment is their low cost and portability. Hence, for HSC to be a viable and potentially widely adoptable sensing strategy, it should ideally be facile to implement in a highly portable format. To this end, we demonstrate in Fig. 7 how HSC-based sensing can be performed with a commercially available handheld RGB module (Versalume). Here, we repeated the measurement of the sample depicted in Fig. 6, *iii* by manually illuminating the sensor with the RGB module and projecting the sample image onto a piece of standard white printer paper as shown in Fig. 7*B*. The handheld nature of the sensor interrogation also conveniently allows for the illumination angle to be varied by the device operator (Movie S6). Snapshots of the sensor response across multiple angles are shown in Fig. 7*C*. As the operating point of the sensor is tuned with illumination angle, the sensitivity can also be varied. This is demonstrated in Fig. 7*C*, *Middle*, as the nonspecific effect of the buffer solution becomes visible by the naked eye for the appropriate configuration. This demonstration shows how HSC-based spatially resolved sensing can be performed in a portable format with low speckle artifacts. In the future, it would be desirable to optimize the sensor design for the exact wavelengths of such a handheld module and to exploit the angular degree of freedom as a means for readily probing a sample across a wide dynamic range and/or manually crossing a PEP.

More generally, a wide variety of structural color sensors, for applications both within and outside biosensing, could be

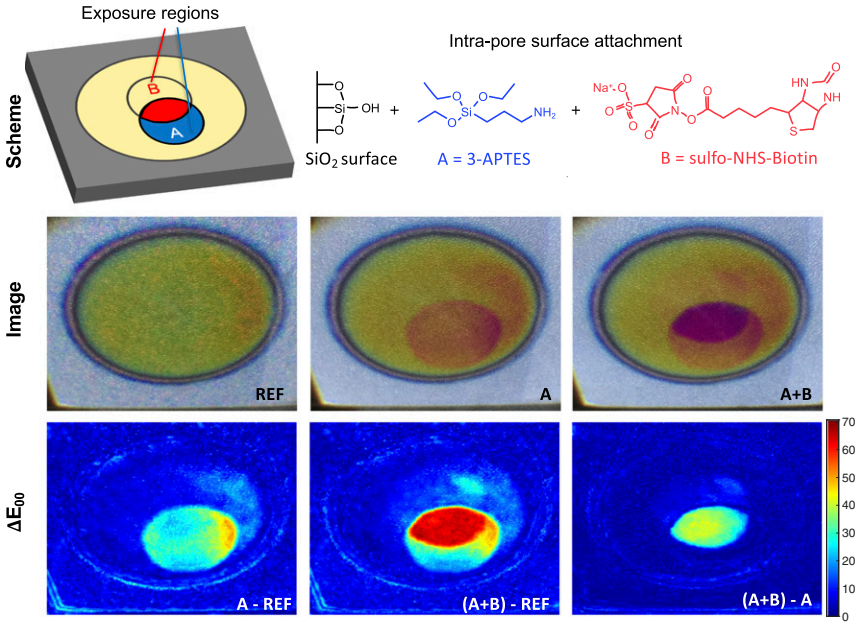

Fig. 5. (*Top*) Schematic of the sensing procedure and intrapore surface attachment chemistry. (*Middle*) Smartphone camera images of the reference (REF), aminopropyltriethoxysilane (APTES) functionalized (A), and biotinylated (A + B) sensor surface in *Left*, *Center*, and *Right*, respectively. (*Bottom*) ΔE_{00} color difference heat map between respective images.

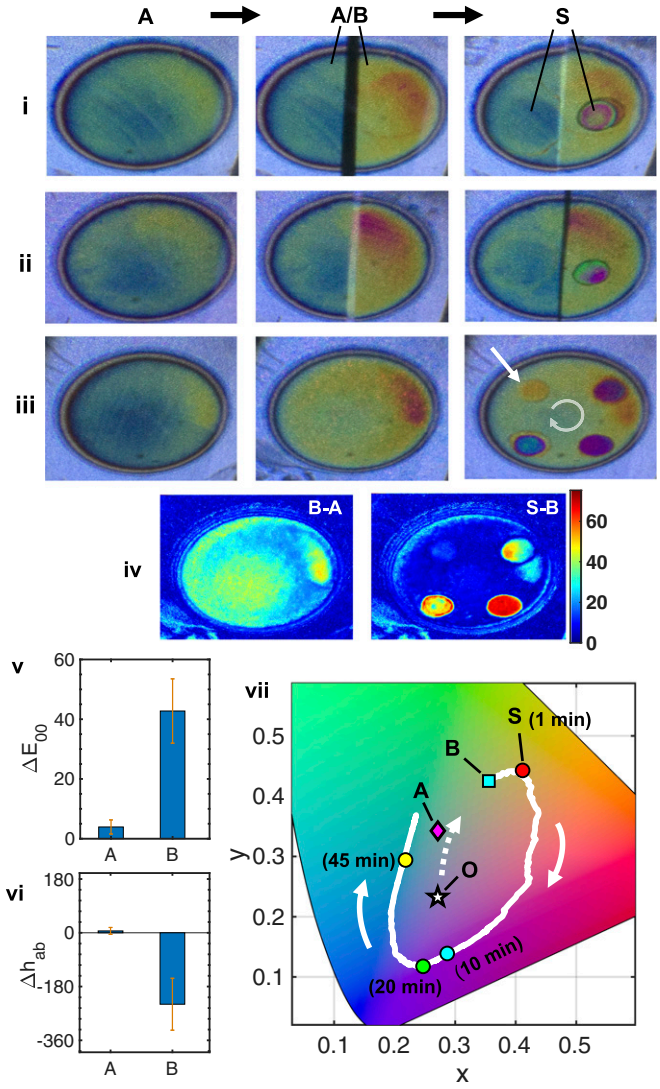

Fig. 6. (*i* and *ii*) Two samples after exposure to 3-APTES (A) and diced in half with the right half exposed to NHS-PEG_4-biotin (B); then, both halves are exposed to streptavidin (S) in the arrow-indicated region to show specificity. (*iii*) A similar sample after exposure to 3-APTES (A) and NHS-PEG_4-biotin (B) and then, exposure to streptavidin for different times. Starting from the pointed arrow going clockwise, the exposure times are 1, 10, 20, and 45 min. (*iv*) ΔE_{00} performed in *iii* before and after biotin (*Left*) and streptavidin (*Right*). (*v*) ΔE_{00} and (*vi*) change of hue (Δh_{ab}) resulting from streptavidin on 3-APTES control (A) and NHS-PEG_4-biotin (B) shown in *i* and *ii*. The change in hue asserts that the change resulting from streptavidin on 3-APTES (A) is corrosive and is confirmed by wavelength shift measurements (blue shift), whereas streptavidin on biotin results in a large red shift. (*vii*) Color trajectory at each stage of surface modification: oxidized (O), 3-APTES (A), NHS-PEG_4-biotin (B), and streptavidin (S) for varying exposure times.

envisioned and measured with this technique, such as those based on other types of etalons and filters including, for example, hydrogel and porous alumina thin films (11, 42). Our analysis suggests that a wide variety of structural color sensors from the literature (10) could benefit from the enhanced sensitivity afforded by the use of multichromatic laser illumination. Alternatively, types of advanced structural color filters and sensors, with customized or pixelated spectral characteristics, could be optimized specifically for HSC and envisioned based upon photonic crystals, grating structures, and dielectric metasurfaces.

Conclusion

In summary, we have presented a general colorimetric sensing technique, HSC, which relies on a structural color filter in combination with a multichromatic laser illuminant. Our approach is specifically motivated for human visual perception as well as color camera imaging, both of which naturally involve the weighting and discrimination of signals arriving from multiple primary photoreceptors (detectors) each with unique spectral properties. When a structural color filter is used as a sensing element, which is spectrally perturbed by an input stimulus, the HSC scheme offers a means for realizing unparalleled color responses owing to an ultrahigh colorimetric sensitivity $\partial E_{00}/\partial\lambda$, which can be tailored to exceed the bounded sensitivities of traditional chromatic sensors by orders of magnitude. Compared against achromatic luminance-based sensors, the added chromatic degrees of freedom of HSC offer a means for enhancing the perceived color response derived from a given optical filter. Hence, HSC offers a foundation for realizing colorimetric devices and sensors with unprecedented colorimetric sensitivities toward input stimuli.

We also experimentally validated the HSC technique and demonstrated how the sensitivity and LOD can be modulated by the choice of structural color filter and/or by actively perturbing the condition of the optical filter. We demonstrated spatially visible label-free detection of small molecules in a large area (approximately centimeters squared2) sensor without the need for any lithographic sensing elements, and we reported a naked eye LOD of ~3 pg mm^{-2}. While our experimental demonstration was focused on label-free biosensing, the HSC technique is significantly more general and can be applied to enhance the color response of colorimetric sensors used in many applications across the physical sciences. We expect that a wide variety of filter types and illumination configurations may be utilized to benefit a growing variety of sensing or device applications such as structural

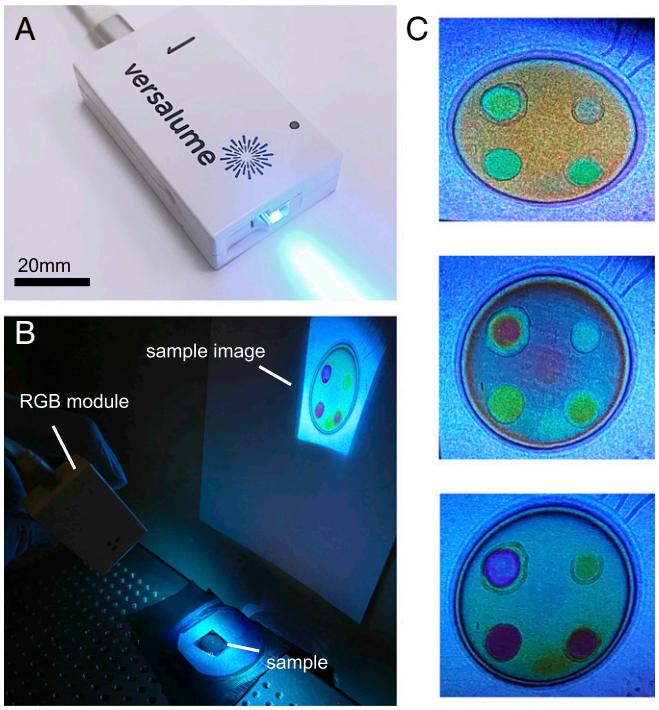

Fig. 7. (*A*) Photograph of a commercially available and handheld RGB laser module. (*B*) The handheld experimental setup showing a simple projection onto a piece of printer paper using the sample previously depicted in Fig. 6, *iii*. (*C*) Images of the sensor as captured at different illumination angles.

and environmental monitoring, multiplexed sensing, and point-of-care diagnostics.

Materials and Methods

Simulations. The thin-film reflectance spectra are simulated using the transfer matrix method (43), where the porous silicon (pSi) thin film is modeled using dispersive Bruggeman effective medium approximation (44). Here, the reflectance values at specific RGB laser wavelengths are extracted followed by color estimation using the pspectro toolkit available for MATLAB (45). From this, the CIE XYZ values that correspond to the thin-film color can be converted to either CIE LAB or RGB color values for display and analysis. The perceptual color difference ΔE_{00} is calculated from the CIE LAB color values (24). Color trajectories and colorimetric sensitivities are simulated by red shifting the structural color spectra in small increments and analyzing the resultant color in CIE color space.

Porous Silicon Fabrication. Double side-polished, boron-doped, p-type <100> silicon wafers (0.01 Ω-cm) are first diced into ∼3 × ∼3-inch dies and then anodized in a 15% ethanoic hydrofluoric acid solution at 42.5-mA/cm^2 current density with a computer-controlled current source (Keithley 2601A) for 40, 43, and 38 s for recipe A, recipe B, and recipe C, respectively. This results in ∼1,140-, ∼1,250-, or ∼1,090-nm-thick pSi thin films with approximately ∼40-nm median pore diameter as determined by cross-sectional scanning electron micrscopy (SEM). The porosity of the films is estimated at ∼75% based on fitting the reflectance spectra to a two-component Bruggeman effective medium model (44). Upon anodization, the sensors are oxidized at 500 °C in air ambient in a preheated Thermo Scientific Lindberg/Blue M Moldatherm Box Furnace (100 °C to 1,100 °C model) for 10 min to prepare for silanization and water vapor adsorption. The approximate oxide thickness is estimated to be ∼4 to 5 nm.

Reflectance Measurement. Reflectance measurements are performed with an Ocean Optics LS-1-LL lamp and an Ocean Optics USB4000 spectrometer over a sample area of 0.5 mm^2 and a wavelength range of ∼400 to 1,100 nm. The RI is calculated by fitting the reflectance spectra of the thin film using the transfer matrix method. The porosity can be extracted from the RI using the Bruggeman effective medium model.

Multichromatic Sample Interrogation. An iPhone 6 is used to capture the images illuminated via a tricolor RGB laser (World Star Tech) coupled to a fiber (Versalume Corning Fibrance) that is collimated through a lens that illuminates the sensor surface. The reflection of the illumination is projected on a white diffuser screen (Thorlabs EDU-VS1) that allows imaging by a smartphone camera or a human eye. The color of this scattered light is angularly invariant to the observer. Captured images and videos are uploaded to a computer and analyzed using MATLAB image processing. Videos are treated as frames of RGB images, and the individual RGB values are analyzed in the CIE color space. The color difference (ΔE_{00}) values are calculated using CIE LAB 2000 formulas (24).

Surface Characterization. 3-APTES was purchased from Acros Organics and used to functionalize the silica surface. For very low concentrations, aminopropyltriethoxysilane diluted in deionized (DI) water is locally applied for ∼5 to 10 s. EZ-Link Sulfo-NHS-Biotin purchased from Thermo Fisher Scientific is diluted in DI water and drop cast on the sensor surface for biotinylation of the sample in Fig. 5. All chemicals used are analytical grade and are used without any further purification.

Biotin–Streptavidin Preparation. Recipe C pSi samples are exposed to 3% 3-APTES in 1:1 methanol:DI water for 25 min. Samples are then rinsed with ethanol, dried in air, and annealed at 100 °C for 10 min. Samples are then exposed to immediately prepared NHS-PEG$_4$-biotin (20 mM) for 1.5 h. After rinsing the sample with ethanol and drying with air, Pierce streptavidin (10 mg/mL), lyophilized in PBS, is first reconstituted in DI water and then, is locally applied to the sample for varying durations of exposure. Afterward, the sample is vigorously rinsed and sonicated in ethanol for 5 min, and then, it is dried in air; 1X PBS is also drop cast in the middle of the sample for 45 min as control.

Handheld RGB Module. The handheld illuminant consists of a Versalume Multi-Color Smart Module with measured wavelengths of 455 nm (blue), 525 nm (green), and 654 nm (red). Light is emitted directly from the module without any fiber attached. The blue and green lasers are TE (transverse electric) polarized, while the red laser is TM (transverse magnetic) polarized. The polarization can be switched or the illumination angle altered by physically rotating the module by hand.

Data Availability. All study data are included in the article and *SI Appendix*.

ACKNOWLEDGMENTS. This work was supported in part by National Science Foundation Grants CMMI-1825787 and OIA-1632881. B.M. and J.D.R. acknowledge Clemson University's Center for Optical Materials Science and Engineering Technologies and Courtney Kucera for organizing the Charles H. Townes Optical Science and Engineering Summer Program.

1. G. Kim *et al.*, Spatially pressure-mapped thermochromic interactive sensor. *Adv. Mater.* **29**, 1606120 (2017).
2. I. R. Howell, C. Li, N. S. Colella, K. Ito, J. J. Watkins, Strain-tunable one dimensional photonic crystals based on zirconium dioxide/slide-ring elastomer nanocomposites for mechanochromic sensing. *ACS Appl. Mater. Interfaces* **7**, 3641–3646 (2015).
3. L. Tong *et al.*, Tunable design of structural colors produced by pseudo-1D photonic crystals of graphene oxide. *Small* **12**, 3433–3443 (2016).
4. C. Chen, G. Song, J. Ren, X. Qu, A simple and sensitive colorimetric pH meter based on DNA conformational switch and gold nanoparticle aggregation. *Chem. Commun. (Camb.)* **46**, 6149–6151 (2008).
5. S. V. Ekkad, J.-C. Han, A transient liquid crystal thermography technique for gas turbine heat transfer measurements. *Meas. Sci. Technol.* **11**, 957–968 (2000).
6. A. A. Yanik *et al.*, Seeing protein monolayers with naked eye through plasmonic Fano resonances. *Proc. Natl. Acad. Sci. U.S.A.* **108**, 11784–11789 (2011).
7. T. Cao, Y. Zhao, C. A. Nattoo, R. Layouni, S. M. Weiss, A smartphone biosensor based on analysing structural colour of porous silicon. *Analyst (Lond.)* **144**, 3942–3948 (2019).
8. Y. Jiang *et al.*, Aptamer/AuNP biosensor for colorimetric profiling of exosomal proteins. *Angew. Chem. Int. Ed. Engl.* **56**, 11916–11920 (2017).
9. L. Xiao *et al.*, Colorimetric biosensor for detection of cancer biomarker by Au nanoparticle-decorated Bi_2Se_3 nanosheets. *ACS Appl. Mater. Interfaces* **9**, 6931–6940 (2017).
10. M. Qin, M. Sun, M. Hua, X. He, Bioinspired structural color sensors based on responsive soft materials. *Curr. Opin. Solid State Mater. Sci.* **23**, 13–27 (2019).
11. M. Qin *et al.*, Bioinspired hydrogel interferometer for adaptive coloration and chemical sensing. *Adv. Mater.* **30**, e1800468 (2018).
12. E.-L. Lin, W.-L. Hsu, Y.-W. Chiang, Trapping structural coloration by a bioinspired gyroid microstructure in solid state. *ACS Nano* **12**, 485–493 (2018).
13. I. B. Burgess *et al.*, Wetting in color: Colorimetric differentiation of organic liquids with high selectivity. *ACS Nano* **6**, 1427–1437 (2012).
14. E. Priyadarshini, N. Pradhan, Gold nanoparticles as efficient sensors in colorimetric detection of toxic metal ions: A review. *Sens. Actuators B Chem.* **238**, 888–902 (2017).
15. K. L. Naughton *et al.*, Self-assembly of the cephalopod protein reflectin. *Adv. Mater.* **28**, 8405–8412 (2016).
16. T. Ogoshi, A. Harada, Chemical sensors based on cyclodextrin derivatives. *Sensors (Basel)* **8**, 4961–4982 (2008).
17. Y. Zhao, Z. Xie, H. Gu, C. Zhu, Z. Gu, Bio-inspired variable structural color materials. *Chem. Soc. Rev.* **41**, 3297–3317 (2012).
18. T. Lee, J. Jang, H. Jeong, J. Rho, Plasmonic- and dielectric-based structural coloring: From fundamentals to practical applications. *Nano Converg.* **5**, 1–21 (2018).
19. X. Zhu, W. Yan, U. Levy, N. A. Mortensen, A. Kristensen, Resonant laser printing of structural colors on high-index dielectric metasurfaces. *Sci. Adv.* **3**, e1602487 (2017).
20. C. Ji *et al.*, Engineering light at the nanoscale: Structural color filters and broadband perfect absorbers. *Adv. Opt. Mater.* **5**, 1700368 (2017).
21. H. Wang, K. Q. Zhang, Photonic crystal structures with tunable structure color as colorimetric sensors. *Sensors (Basel)* **13**, 4192–4213 (2013).
22. K. Kumar *et al.*, Printing colour at the optical diffraction limit. *Nat. Nanotechnol.* **7**, 557–561 (2012).
23. W. Yang *et al.*, All-dielectric metasurface for high-performance structural color. *Nat. Commun.* **11**, 1864 (2020).
24. G. Sharma, W. Wu, E. N. Dalal, The CIEDE2000 color-difference formula: Implementation notes, supplementary test data, and mathematical observations. *Color Res. Appl.* **30**, 21–30 (2005).
25. G. Sharma, R. Bala, *Digital Color Imaging Handbook* (CRC Press, 2017).
26. O. Burggraaff *et al.*, Standardized spectral and radiometric calibration of consumer cameras. *Opt. Express* **27**, 19075–19101 (2019).
27. V. S. Y. Lin, K. Motesharei, K. P. S. Dancil, M. J. Sailor, M. R. Ghadiri, A porous silicon-based optical interferometric biosensor. *Science* **278**, 840–843 (1997).
28. S. Arshavsky-Graham, N. Massad-Ivanir, E. Segal, S. Weiss, Porous silicon-based photonic biosensors: Current status and emerging applications. *Anal. Chem.* **91**, 441–467 (2019).
29. M. M. Orosco, C. Pacholski, M. J. Sailor, Real-time monitoring of enzyme activity in a mesoporous silicon double layer. *Nat. Nanotechnol.* **4**, 255–258 (2009).
30. H. Ouyang, C. C. Striemer, P. M. Fauchet, Quantitative analysis of the sensitivity of porous silicon optical biosensors. *Appl. Phys. Lett.* **88**, 1–4 (2006).
31. T. H. Talukdar, G. D. Allen, I. Kravchenko, J. D. Ryckman, Single-mode porous silicon waveguide interferometers with unity confinement factors for ultra-sensitive surface adlayer sensing. *Opt. Express* **27**, 22485–22498 (2019).

32. S. TalebiFard *et al*., *Optimized sensitivity* of Silicon-on-Insulator (SOI) strip waveguide resonator sensor. *Biomed. Opt. Express* **8**, 500–511 (2017).
33. T. Chung, S. Y. Lee, E. Y. Song, H. Chun, B. Lee, Plasmonic nanostructures for nano-scale bio-sensing. *Sensors (Basel)* **11**, 10907–10929 (2011).
34. B. Redding, M. A. Choma, H. Cao, Speckle-free laser imaging using random laser illumination. *Nat. Photonics* **6**, 355–359 (2012).
35. U. Jönsson *et al*., Real-time biospecific interaction analysis using surface plasmon resonance and a sensor chip technology. *Biotechniques* **11**, 620–627 (1991).
36. D. Wang *et al*., Real-time multi-channel SPR sensing based on DMD-enabled angular interrogation. *Opt. Express* **26**, 24627–24636 (2018).
37. M. R. Gartia *et al*., Colorimetric plasmon resonance imaging using nano lycurgus cup arrays. *Adv. Opt. Mater.* **1**, 68–76 (2013).
38. S. Chun, G. M. Miskelly, Hyperspectral and color imaging of solvent vapor sorption into porous silicon. *Front Chem.* **6**, 610 (2018).
39. F. Yesilkoy *et al*., Ultrasensitive hyperspectral imaging and biodetection enabled by dielectric metasurfaces. *Nat. Photonics* **13**, 390–396 (2019).
40. J. E. Garcia *et al*., Differentiating biological colours with few and many sensors: Spectral reconstruction with RGB and hyperspectral cameras. *PLoS One* **10**, e0125817 (2015).
41. Y. Zhuo, B. T. Cunningham, Label-free biosensor imaging on photonic crystal surfaces. *Sensors (Basel)* **15**, 21613–21635 (2015).
42. S. D. Alvarez, C. P. Li, C. E. Chiang, I. K. Schuller, M. J. Sailor, A label-free porous alumina interferometric immunosensor. *ACS Nano* **3**, 3301–3307 (2009).
43. K. Ohta, H. Ishida, Matrix formalism for calculation of electric field intensity of light in stratified multilayered films. *Appl. Opt.* **29**, 1952–1959 (1990).
44. T. H. Talukdar, J. C. Perez, J. D. Ryckman, Nanoimprinting of refractive index: Patterning subwavelength effective media for flat optics. *ACS Appl. Nano Mater.* **3**, 7377–7383 (2020).
45. M. Aldrich, pspectro: Photometric and Colorimetric Calculations, MATLAB Central File Exchange. MATLAB Central File Exchange. Version 1.2.0.0. https://www.mathworks.com/matlabcentral/fileexchange/28185-pspectro-photometric-and-colorimetric-calculations. Accessed 17 October 2020.